Key Points:
- Cusp plasma density correlates well with solar wind plasma density
- Cusp soft electron precipitations correlates best with SW dynamic pressure
- The direct-entry cusp soft electron exhibits hemispheric asymmetry at solstice

On the Relation Between Soft Electron Precipitations in the Cusp Region and Solar Wind Coupling Functions

Tong Dang[1,2] (ID), Binzheng Zhang[2] (ID), Michael Wiltberge[2], Wenbin Wang[2] (ID), Roger Varney[3] (ID), Xiankang Dou[1] (ID), Weixing Wan[4], and Jiuhou Lei[1] (ID)

[1]CAS Key Laboratory of Geospace Environment, School of Earth and Space Sciences, University of Science and Technology of China, Hefei, China, [2]High Altitude Observatory, National Center for Atmospheric Research, Boulder, CO, USA, [3]Center for Geospace Studies, SRI International, Menlo Park, CA, USA, [4]Institute of Geology and Geophysics, Chinese Academy of Sciences, Beijing, China

Abstract In this study, the correlations between the fluxes of precipitating soft electrons in the cusp region and solar wind coupling functions are investigated utilizing the Lyon-Fedder-Mobarry global magnetosphere model simulations. We conduct two simulation runs during periods from 20 March 2008 to 16 April 2008 and from 15 to 24 December 2014, which are referred as "Equinox Case" and "Solstice Case," respectively. The simulation results of Equinox Case show that the plasma number density in the high-latitude cusp region scales well with the solar wind number density ($n_{cusp}/n_{sw} = 0.78$), which agrees well with the statistical results from the Polar spacecraft measurements. For the Solstice Case, the plasma number density of high-latitude cusp in both hemispheres increases approximately linearly with upstream solar wind number density with prominent hemispheric asymmetry. Due to the dipole tilt effect, the average number density ratio n_{cusp}/n_{sw} in the Southern (summer) Hemisphere is nearly 3 times that in the Northern (winter) Hemisphere. In addition to the solar wind number density, 20 solar wind coupling functions are tested for the linear correlation with the fluxes of precipitating cusp soft electrons. The statistical results indicate that the solar wind dynamic pressure p exhibits the highest linear correlation with the cusp electron fluxes for both equinox and solstice conditions, with correlation coefficients greater than 0.75. The linear regression relations for equinox and solstice cases may provide an empirical calculation for the fluxes of cusp soft electron precipitation based on the upstream solar wind driving conditions.

1. Introduction

The polar cusp provides direct access for solar wind (SW) plasma of the magnetosheath into the magnetosphere and the ionosphere at low altitudes (e.g., Heikkila & Winningham, 1971). The direct-entry electrons in the polar cusp region have a relatively soft energy (approximately several hundred eV) compared with those of precipitating monoenergetic and diffuse electrons (approximately several keV). Over the decades, the soft electron precipitation in the cusp region have been observed by both ground-based instruments (Eather, 1985) and in situ satellite measurements (Newell et al., 1989, 2009; Smith & Lockwood, 1996), suggesting that the energy of these direct-entry soft electrons is similar to the typical values in the magnetosheath.

Direct-entry soft electron precipitation plays an important role in multiple physical processes within the coupled ionosphere-thermosphere system, depositing energy by heating ionospheric plasma through collisions and enhancing the ionization and conductivity at F region altitudes (Rentz, 2009). For instance, the ions in the cusp region are suggested to be accelerated by parallel electric fields which are established by precipitating soft electrons, which is known as the type 2 ion upflow (Burchill et al., 2010; Ogawa et al., 2003; Skjæveland et al., 2011; Strangeway et al., 2005; Wahlund et al., 1992). Studies have also shown that soft electron precipitation has a prominent impact on the thermospheric density enhancement in the cusp region, through changing the F region ionization and conductivity above 150 km and further influencing the altitudinal distribution of Joule heating rates (Deng et al., 2013; Rentz, 2009; Zhang et al., 2012; Zhang, Varney, et al., 2015).

A number of SW coupling functions have been used extensively to describe the SW-magnetosphere interactions and magnetosphere-ionosphere coupling processes, including the location of the polar cusp (e.g., Borovsky, 2013; Kan & Lee, 1979; McPherron et al., 2015; Newell et al., 2007; Perreault & Akasofu, 1978). The most commonly used SW coupling functions in the literature are the variations of the SW electric field vB_T (e.g., Kan & Lee, 1979; Scurry & Russell, 1991; Vasyliunas et al., 1982; Wygant et al., 1983), where v is the SW velocity and B_T is $\sqrt{b_z^2 + b_y^2}$. These SW coupling functions work well for the hard electron precipitations (such as the OVATION aurora model (Newell et al., 2002, 2014)) since the electrodynamic processes play a great role in the plasma sheet and magnetotail. However, the SW coupling functions may not work well in the soft electron precipitations. Due to the lack of long-term measurements in the cusp region, it is difficult to study these correlations from the observations. Recently, Walsh et al. (2016) investigated the plasma density variations in the high-altitude cusp region using 7 years of measurements from the Polar spacecraft and the statistical results showed that the plasma number density in the high-altitude cusp region scales well with the solar wind number density (n_{cusp}/n_{sw} ˜ 0.8) with a linear correlation of 0.78 for radial distances greater than 4 R_E. Their results suggest that the plasma density of the SW might be an important parameter for describing the direct-entry cusp electrons, which is not included in most SW coupling functions based on the SW electric field. Therefore, it is necessary to investigate whether these SW coupling functions with the electric field involved can be extended to describe the direct-entry cusp soft electron precipitation and test the hypothesis that the SW number density is a critical parameter for direct-entry soft electrons in the cusp region as suggested by Walsh et al. (2016).

In this study, we investigate the relationship between solar wind conditions and cusp number density at high-altitude (radial distance of 5 R_E) using the Lyon-Fedder-Mobarry (LFM) global magnetosphere model based on two event simulations near March equinox and December solstice, respectively. The simulated relationship between solar wind number density and cusp number density is in agreement with the statistical results derived by Walsh et al. (2016). With the implementation of a direct-entry cusp electron precipitation model, the effectiveness of various SW coupling functions are tested using the simulated number flux and energy flux of cusp soft electron, for both the equinox and the solstice cases. In section 2, we describe the information of LFM global MHD model and SW/interplanetary magnetic field (IMF) conditions for the two event simulations. Sections 3 and 4 show the simulation results and the discussions about the effect of ionospheric outflow. We summarize the results in section 5.

2. Simulation Information

2.1. The LFM Model

The LFM global model has been widely utilized to investigate the interactions between solar wind, magnetosphere, and ionosphere. A high-order, finite volume total variation diminishing scheme is used in the LFM simulation to solve the single-fluid ideal MHD equations. In the solar magnetospheric (SM) coordinates (X_{SM}, Y_{SM}, Z_{SM}), the simulation domain of the LFM model has a range of $-300R_E \leq X_{SM} \leq 30R_E$ and $-100R_E \leq Y_{SM}, Z_{SM} \leq 100R_E$. The bottom boundary of the model is nearly a spherical surface at a radial distance of 2 R_E. In the high-altitude region where the cusp locations are calculated in the following sections, the grid spacing is approximately 0.4 R_E in the radial direction. The detailed description of the LFM model can be seen in Lyon et al. (2004) and Merkin and Lyon (2010).

The cusp electron precipitation model implemented in the LFM global code is described in detail in Zhang, Lotko, et al. (2015). Here we provide the basic calculation of the number flux and energy flux of the precipitating cusp electrons in the global model. Based on the identification of the cusp area (see Zhang et al., 2013), the number flux F_N and energy flux F_E of precipitating direct-entry cusp electrons are calculated as

$$F_N = L_0 \frac{N_e T_e^{1/2}}{\sqrt{2\pi m_e}} \qquad (1)$$

$$F_E = 2F_N T_e \qquad (2)$$

where m_e is the electron mass. N_e and T_e are the electron number density and temperature in the high-altitude cusp region, respectively. In the event simulations, the N_e and T_e are calculated at a fiducial surface of 5 R_E. The empirical parameter L_0 represents the degree of loss cone filling in the electron source region. Since cusp flux tubes are assumed to be continuously refilled by solar wind plasma, a full loss cone is used in this study. In this
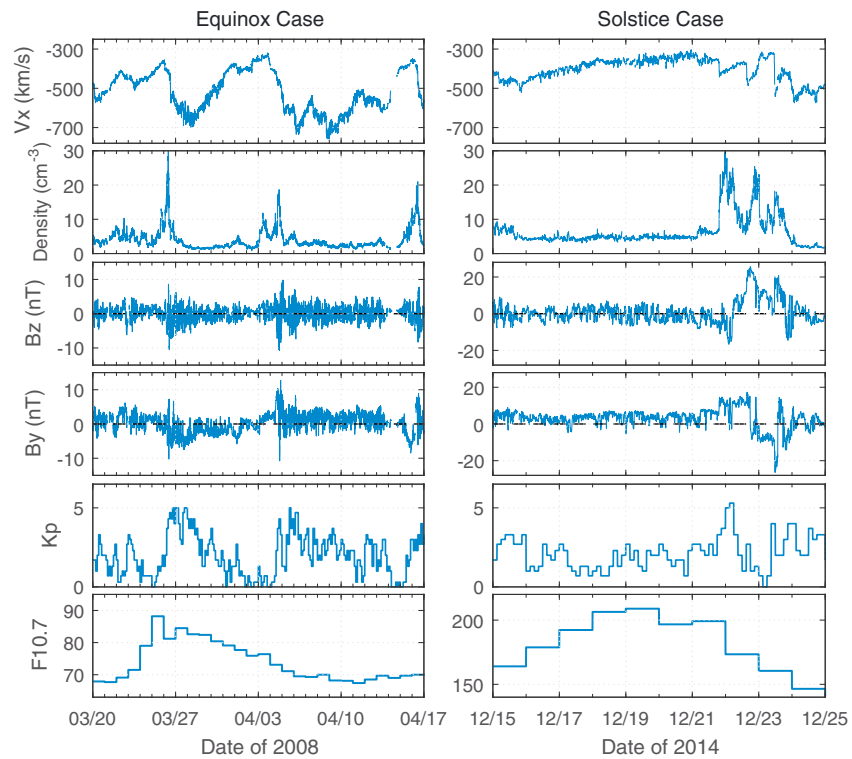
Figure 1. Variations of SW/IMF conditions for the events of (left column) Equinox Case and (right column) Solstice Case, respectively.

study, we consider all the electrons in the cusp region where the soft electrons are the majority. In the global simulation, soft electron precipitation is differentiated from monoenergy and diffuse electron precipitations which are usually in the keV range. The modeled direct-entry cusp electron precipitation usually represents the magnetosheath temperature ranging from approximately 100 eV to 500 eV depending on the upstream driving conditions. The details about the properties of the direct-entry cusp electron precipitation can be found in Zhang, Lotko, et al. (2015).

2.2. Two Event Simulations

Two simulations are conducted from 20 March 2008 to 16 April 2008 and from 15 to 24 December 2014, which are referred as the Equinox Case and the Solstice Case in the following sections, respectively. Both simulations use the standard LFM grid with $53 \times 48 \times 64$ cells. The simulation data are recorded at a time resolution of 2 min. Figure 1 shows the SW and interplanetary magnetic field (IMF) for the Equinox Case and the Solstice Case, respectively. The SW data covers a reasonable range for a linear correlation analysis, for example, for the Equinox Case, the SW velocity varies from -700 km/s to -300 km/s and the SW density has a range from 2 cm^{-3} to 30 cm^{-3}. These two event simulations provide a reasonable statistical ensemble for determining the correlation between the simulated direct-entry cusp soft electron precipitation and the upstream SW parameters, especially the SW density and dynamic pressure which are ignored in most SW coupling functions. In both event simulations, the geomagnetic activity level was relatively low: the Kp index was less than 5 and no major magnetic storms occurred during the two intervals. The Equinox Case is near the solar minimum, with a mean $F_{10.7}$ value of about 80 (solar flux unit, sfu). The Solstice Case has a much higher solar activity and the $F_{10.7}$ index is above 150 (sfu). The minimum, mean, and maximum values of the SW/IMF conditions derived from the two cases are summarized in Table 1. In this study, the solar wind data at the nose point of the bow shock are compared with the cusp direct-entry electron precipitations.

3. Results

3.1. Cusp Density Versus SW Density

3.1.1. The Equinox Case

In order to compare the simulation results with Walsh et al. (2016), we apply the cusp identification algorithm developed by Zhang et al. (2013) to calculate the average cusp number density at different altitudes in the

Table 1
The Minimum, Mean, and Maximum Value of Solar Wind, IMF, and Geomagnetic Data for the "Equinox Case" and "Solstice Case"

Name	Equinox Case (Min, Mean, Max)	Solstice Case (Min, Mean, Max)
V_x (km/s)	−758.7, −515.5, −319.9	−574.3, −403.0, −304.1
Density (cm^{-3})	0.81, 4.0, 31.1	1.4, 6.5, 30.4
B_z (nT)	−10.7, 0.1, 9.8	−16.7, 0.9, 25.7
B_y (nT)	−10.8, 0.3, 12.7	−26.4, 3.0, 17.3
Kp	0, 2.0, 5.0	0, 2.1, 5.3
$F_{10.7}$	67.4, 73.8, 88.2	140.6, 182.7, 208.9

LFM simulation. Figure 2 shows the simulated relationship between the average cusp plasma number density at a radial distance of 5 R_E and the solar wind number density in the Northern Hemisphere and Southern Hemisphere derived from the Equinox Case, respectively. The cusp number density n_{cusp} averaged within the high-altitude cusp region at a radial distance of 5 R_E. The dipole tilt effect on the linear correlation between the simulated n_{cusp} and n_{sw} is relatively small. As shown in Figure 2a, in the Northern Hemisphere, the average number density in the high-altitude cusp region increases approximately linearly with the solar wind number density with a correlation coefficient of 0.91, which indicates the efficient direct entry of solar wind plasma into the high-altitude cusp region in the simulation. The ratio between the cusp number density and SW number density is 0.78 in the global simulation, which agrees well with the ratio of 0.8 in the observations of Walsh et al. (2016), which is averaged over all seasons and dipole tilt conditions. Note that since the Polar's orbit passes through the noon-midnight meridian twice per year (once with perigee toward noon and once with apogee toward noon), the condition of being within 1.5 h of local noon is met during two periods each year, one in March–April and the other in September–October. Therefore, the equinox simulation will better represent the Polar data than the solstice simulation. As compared with Figure 2a, the simulated cusp number density in the Southern Hemisphere shown in Figure 2b still scales well with the SW number density. However, the mean density ratio n_{cusp}/n_{sw} is 0.53, which is lower than the ratio of 0.78 in the Northern Hemisphere. This could be explained by the dipole tilt effect caused by the time period used in the Equinox Case simulation. The simulation period is not centered on the March equinox but moves into April. As a consequence, the Northern Hemisphere tilts more toward the Sun, leading to a larger plasma density ratio n_{cusp}/n_{sw} than that in the Southern Hemisphere.

Figure 3 shows the simulated density ratio (n_{cusp}/n_{sw}) derived from the high-altitude cusp region in two hemispheres as a function of geocentric radial distance derived from the Equinox Case simulation. The red band inside the box is the median value, while the bottom and top of the box represent the first and third quartiles of
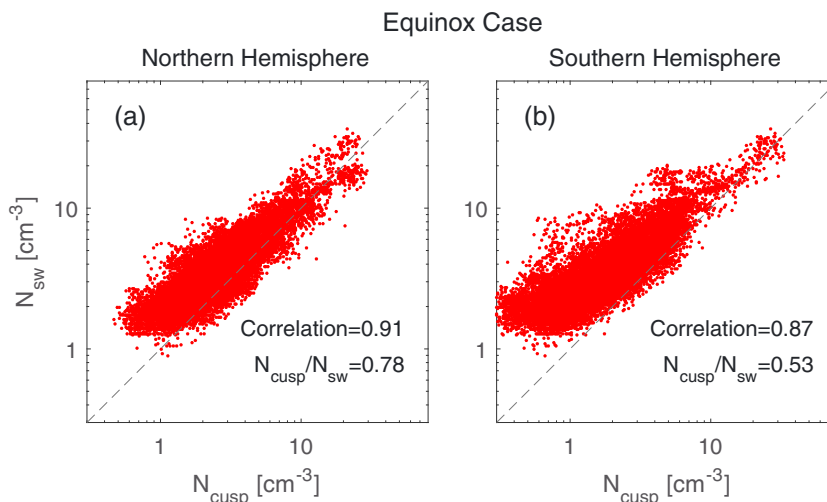

Figure 2. Plasma number density within the cusp at a radial distance of 5 R_E in the (a) Northern Hemisphere and (b) Southern Hemisphere as a function of solar wind number density derived from the Equinox Case.
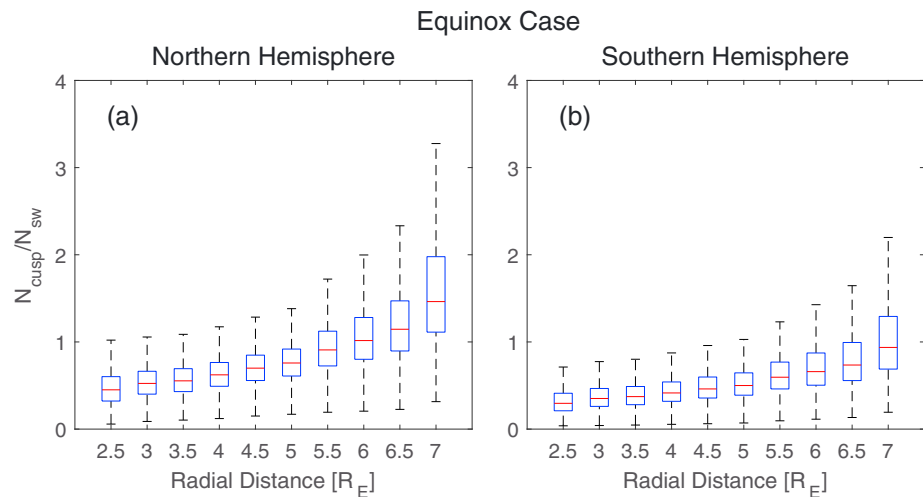
Figure 3. Ratio of cusp plasma number density and solar wind plasma number density as a function of radial distance in the (a) Northern Hemisphere and (b) Southern Hemisphere derived from the Equinox Case.

n_{cusp}/n_{sw}. The whiskers indicate 1.5 times the interquartile range. As shown in Figure 3a, the simulated density ratio n_{cusp}/n_{sw} in the Northern Hemisphere increases from 0.46 to 1.42 as the radial distance increases from 2.5 R_E to 7 R_E. The simulated n_{cusp}/n_{sw} ratio at the radial distances greater than 4 R_E agrees with the measured plasma density ratio variations in Walsh et al. (2016). At radial distances smaller than 4 R_E, the density ratio in the Equinox Case simulation asymptotes to approximately 0.5, which is significantly lower than the observed ratio around 1 – 4. This is due to the absence of ionospheric plasma population at low altitudes in the LFM simulations. Multifluid global simulations have shown that the inclusion of a cold ionosphere population at low altitudes brings the plasma density ratio closer to the observed values below radial distances of 4 R_E (Walsh et al., 2016). The single-fluid LFM simulation uses the "hard wall" boundary condition for magnetospheric plasma such that the cold "de facto outflow" population (Welling & Liemohn, 2014) does not contribute to the plasma density at low altitudes. The radial variation of the simulated n_{cusp}/n_{sw} in the Southern Hemisphere is similar to that in the Northern Hemisphere, but with lower magnitudes. The simulated density ratio n_{cusp}/n_{sw} in the Southern Hemisphere increases from 0.30 to 0.94 as the radial distance increases from 2.5 R_E to 7 R_E.

3.1.2. The Solstice Case

The location and spatial extension of the polar cusp are regulated by the dipole tilt angle (e.g., Zhou et al., 1999). Solar wind more easily enters the hemisphere which is tilted toward the Sun, especially during southward IMF driving. As a consequence, hemispheric asymmetry in the relation between solar wind plasma and cusp plasma is expected at solstice when the dipole tilt angle is large. Figure 4 shows the simulated solar wind number density versus cusp plasma number density in the Northern Hemisphere and the Southern Hemisphere derived from the Solstice Case. The average plasma number density ratio in the Southern (summer) Hemisphere is 0.79, which is much larger than that in the Northern (winter) Hemisphere. The simulation results suggest that at solstice, the winter hemisphere tilts away from the Sun and the entry of solar wind plasma becomes less efficient, with only a plasma number density ratio of 0.24. Note that the simulated high-altitude cusp plasma number density from both hemispheres shows high correlations with the solar wind number density, with correlation coefficients of 0.8 (north) and 0.88 (south). Further observational studies are necessary to verify the simulated hemispheric asymmetry associated with the direct entry of plasma under solstice conditions.

Figure 5 shows the simulated plasma density ratio (n_{cusp}/n_{sw}) as a function of radial distance in two hemispheres derived from the Solstice Case simulation. The simulated density ratios in both hemispheres increase as the radial distance increases, which is similar to the results derived from the Equinox Case. The n_{cusp}/n_{sw} ratio in the Northern (winter) Hemisphere increases from 0.2 to 0.4 as the radial distance increases from 2.5 R_E to 7 R_E. In the Southern (summer) Hemisphere, the simulated density ratio n_{cusp}/n_{sw} has a much larger value than that in the winter hemisphere, which increases from 0.34 to 1.67 as the radial distance increases from 2.5 R_E to 7 R_E. As discussed in the previous section, the absence of ionospheric contribution again leads to a low n_{cusp}/n_{sw} ratio at radial distances less than 4 R_E as in the Equinox Case.
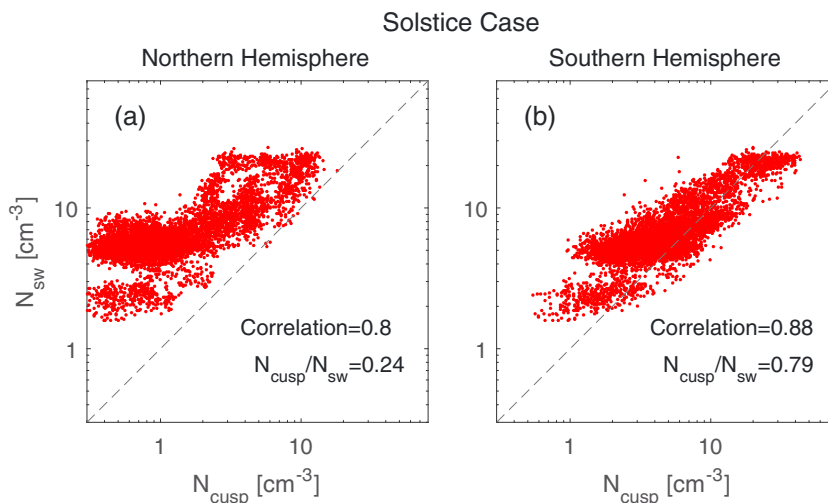
Figure 4. Same as Figure 2 but for the Solstice Case.

Figure 6 shows the plasma density distribution in the *X-Z* plane at 00:00 UT on 21 March 2008 and 21 December 2014, respectively. Both cases exhibit direct entry of plasma from magnetosheath to the high-altitude cusp region. As shown in Figure 6a, the plasma density in the Equinox Case shows a hemispherically symmetric distribution in the magnetosheath, which is the source region of the direct-entry plasma in the high-altitude polar cusp. The plasma in Figure 6a has a maximum density of about 19 cm^{-3}. However, for the Solstice Case with large dipole tilt angle, prominent hemispheric asymmetry can be seen in the plasma distribution in Figure 6b. The plasma density in the Southern Hemisphere is nearly 2–3 times of that in the Northern Hemisphere. This is consistent with the results of plasma density ratio n_{cusp}/n_{sw} in two hemispheres in Figure 5. Note that in Figure 6 the magnetopause location is different in two cases due to the difference of SW/IMF conditions.

3.2. Cusp Electron Precipitation Versus SW Coupling Functions

The above results show that the LFM results generally agrees with the observations of Walsh et al. (2016), both in the high correlation between the cusp plasma number density and solar wind plasma number density and the mean plasma density ratio n_{cusp}/n_{sw}. This suggests that the LFM global model is able to simulate the source region plasma density appropriately. In this subsection, we investigate the relationship between cusp
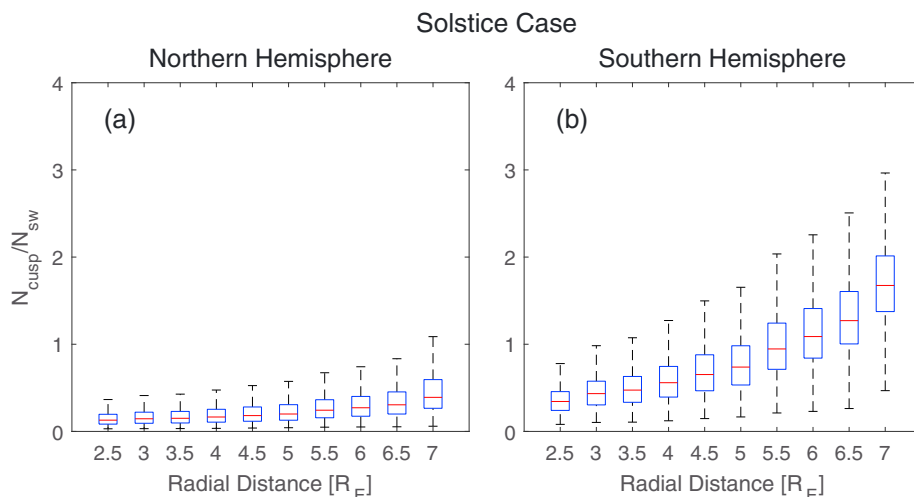

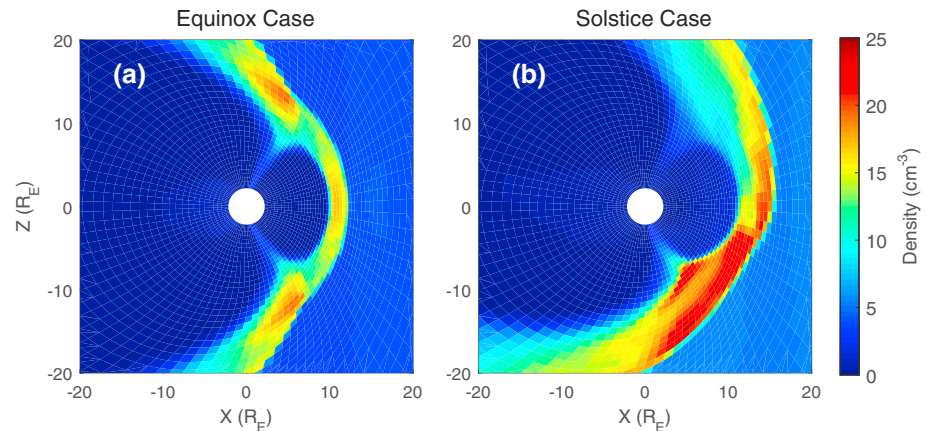**Figure 5.** Same as Figure 3 but for the Solstice Case.

Figure 6. The distribution of plasma density in the *X-Z* plane for the Equinox Case and Solstice Case.

electron precipitations and various SW coupling functions. The hemispheric electron precipitation rate and power are calculated by the hemispheric integration of the electron number flux and energy flux over the cusp region, respectively.

3.2.1. The Equinox Case

Figure 7 displays the linear correlations between the simulated hemispheric integrated rate of the precipitating cusp electrons and the upstream solar wind electric field (vB_T), number density, dynamic pressure (p), and $d\Phi_{MP}/dt$ in the Northern Hemisphere derived from the Equinox Case. The dayside merging rate $d\Phi_{MP}/dt$, which is expressed as ($v^{4/3}B_T^{2/3}\sin^{8/3}(\theta_c/2)$), was proposed by Newell et al. (2007) to be the optimal SW coupling function to predict magnetospheric indices. Results of linear correlation analysis in Figure 7 show that the dynamic pressure and number density significantly higher linear correlation coefficients than the SW electric field and $d\Phi_{MP}/dt$. The SW number density and dynamic pressure have linear correlation coefficients of 0.79 and 0.77, while the correlation coefficients are 0.43 and 0.31 for the solar wind electric field and $d\Phi_{MP}/dt$, respectively. The results indicate that the hemispheric integrated precipitation rate of cusp soft electrons may depend more on the SW plasma number density and dynamic pressure rather than the electric field, suggesting that the direct-entry process is less affected by the electromagnetic coupling process between the SW and magnetosphere than the SW drivers.

Figure 8 shows the linear correlations between the simulated hemispheric power of precipitating cusp soft electrons and the upstream solar wind electric field, number density, dynamic pressure, and $d\Phi_{MP}/dt$ in the Northern Hemisphere for the Equinox Case. Note that the simulated soft electron precipitation within the cusp region has a hemispheric power around 0.1 – 1 GW, which is much less than the total precipitating hemispheric power in the simulation. Once again the dynamic pressure has the highest linear correlation of 0.75 with the hemispheric cusp precipitation power. Compared with the results shown in Figures 7a and 7d, the solar wind electric field and $d\Phi_{MP}/dt$ give better correlations with the hemispheric power than those with the hemispheric precipitation rate. However, the SW number density, which gives the highest correlation with the soft electron precipitation rate, only correlates the hemispheric power with a correlation coefficient of 0.51.

We also performed linear correlation analysis using the SW coupling functions listed in Newell et al. (2007). Table 2 lists the linear correlations between these 20 SW coupling functions and the simulated hemispheric rate and of precipitating cusp soft electrons based on the Equinox Case simulation. The highest linear correlation between the soft electrons and SW coupling function is with the SW dynamic pressure. As expected, the direct-entry cusp electron precipitation rate correlates better with the coupling functions which contain the number density (such as E_{WV} and E_{TL}), while the hemispheric power of soft electrons correlates better with the SW velocity. The linear regression relations between SW dynamic pressure and hemispheric power and hemispheric precipitation rate of cusp soft electrons derived from the Equinox Case in the Northern Hemisphere are

$$\text{Power} = (0.266p \pm 0.003) - (0.110 \pm 0.006) \tag{3}$$

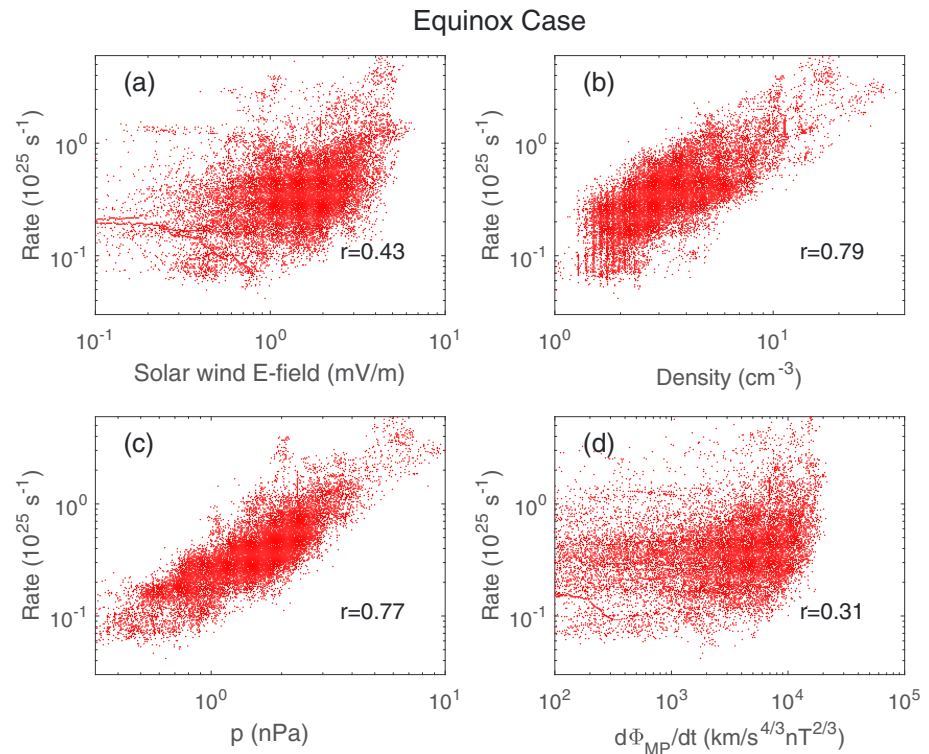$$\text{Rate} = (0.425p \pm 0.005) - (0.214 \pm 0.009) \tag{4}$$

Figure 7. Scatterplots of hemispheric precipitation rate of soft electrons versus solar wind electric field, density, dynamic pressure, and $d\Phi_{MP}/dt$ in the Northern Hemisphere derived from the Equinox Case.

where p (in unit of nanopascals) denotes the SW dynamic pressure and Power (in unit of GW) and Rate (in unit of 10^{25} s^{-1}) represent the hemispheric power and hemispheric precipitation rate of precipitating soft electrons, respectively.

3.2.2. The Solstice Case

The linear correlation analysis discussed in the previous section suggests that the SW dynamic pressure has the highest correlation coefficients with the direct-entry cusp electron precipitation during equinox. In this section we investigate the corresponding linear correlation during solstice conditions. Figure 9 shows the relationship between SW dynamic pressure and hemispheric precipitation rate and hemispheric power of cusp soft electrons derived from the Solstice Case simulation. Results show that the SW dynamic pressure correlates well with hemispheric precipitation rate and hemispheric power in both hemispheres, with linear correlations greater than 0.8. Note that simulated the soft electron precipitation in the cusp region of the winter hemisphere still has a good correlation with the SW dynamic pressure, although the n_{cusp}/n_{sw} ratio is only 0.24 as shown in Figure 4. As a consequence, the magnitudes of the hemispheric precipitation rate and the hemispheric power of cusp soft electrons in the winter hemispheric are significantly lower than those in the summer hemisphere.

Table 3 shows the linear correlations between the simulated hemispheric precipitation rate and hemispheric power of cusp soft electrons and the 20 SW coupling functions listed in Table 2 derived from the Solstice Case in the Northern and the Southern Hemisphere, respectively. Similar to the results derived from the Equinox Case, the dynamic pressure p has the highest linear correlation coefficient for the hemispheric integrated precipitation rate and power in both hemispheres regardless of the dipole tile angle. The plasma number density has the second highest linear correlation coefficient in the 20 SW coupling functions. In the Solstice Case, the solar wind electric field vB_T has significantly higher linear correlation coefficient compared to the results in the Equinox Case, especially on the hemispheric precipitation rate. Hemispheric asymmetries are evident in the correlation coefficients listed in Table 2, which suggests that most SW coupling functions correlate better with the cusp soft electron precipitation in the summer hemisphere than those in the winter hemisphere, except B_z, SW velocity, and SW electric field.
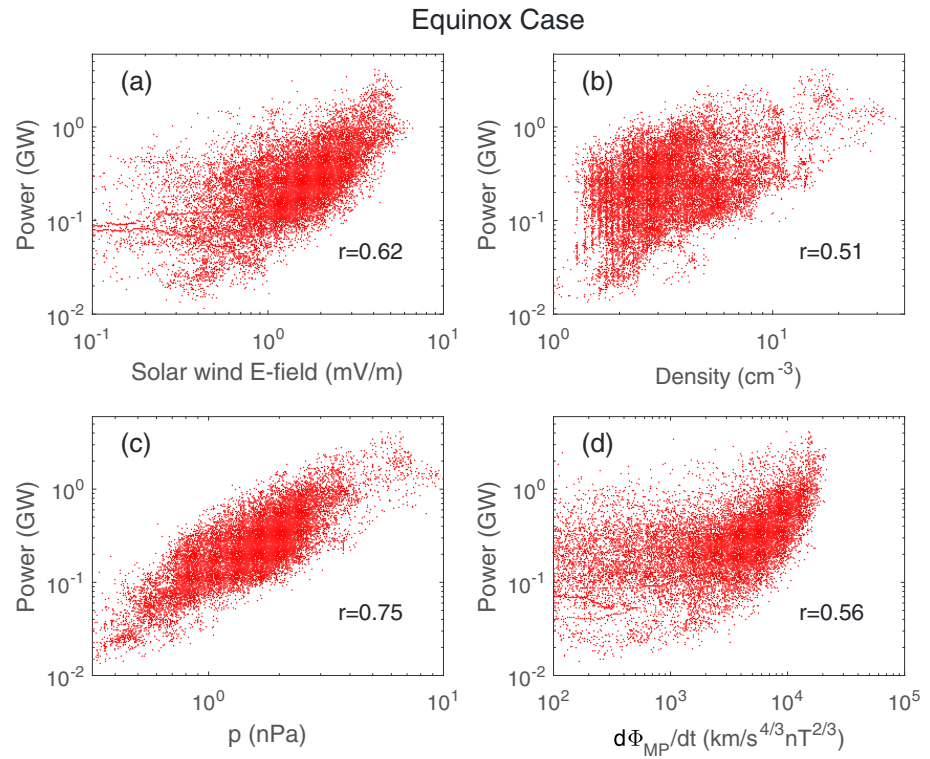
Figure 8. Same as Figure 7 but with the hemispheric power as the *y* axis.

Table 2
The Linear Correlation Between SW Coupling Functions and Cusp Soft Electron Hemispheric Precipitation Rate and Hemispheric Power Derived From the Equinox Case Simulation

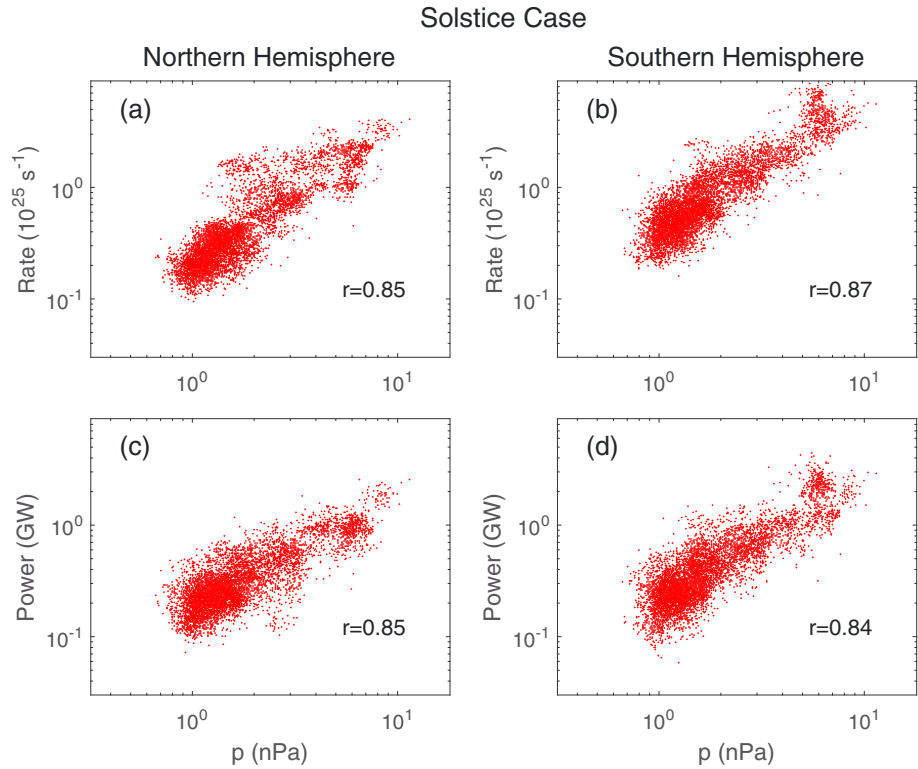| Name	Function form	Hemispheric precipitation rate	Hemispheric power
B_z	B_z	−0.27	−0.38
Velocity	v	−0.15	0.22
Density	n	0.79	0.51
p	$nv^2/2$	0.77	0.75
B_s	$B_z \quad (B_z < 0)$	−0.46	−0.56
	$0 \quad (B_z > 0)$		
Half-wave rectifier	vB_s	−0.39	−0.58
ε	$vB^2 \sin^4(\theta_c/2)$	0.53	0.68
ε_1	$vB_T^2 \sin^4(\theta_c/2)$	0.53	0.68
ε_2	$vB \sin^4(\theta_c/2)$	0.41	0.61
Solar wind E field	vB_T	0.43	0.62
E_{KL}	$vB_T \sin^2(\theta_c/2)$	0.42	0.64
$E_{KL}^{1/2}$	$[vB^2 \sin^2(\theta_c/2)]^{1/2}$	0.36	0.56
E_{KLV}	$v^{4/3}B_T \sin^2(\theta_c/2)p^{1/6}$	0.45	0.68
E_{WAV}	$vB_T \sin^4(\theta_c/2)$	0.41	0.61
E_{WAV}^2	$[vB_T \sin^4(\theta_c/2)]^2$	0.43	0.62
$E_{WAV}^{1/2}$	$[vB_T \sin^4(\theta_c/2)]^{1/2}$	0.35	0.54
E_{WV}	$v^{4/3}B_T \sin^4(\theta_c/2)p^{1/6}$	0.43	0.65
E_{SR}	$vB_T \sin^4(\theta_c/2)p^{1/6}$	0.55	0.73
E_{TL}	$n^{1/2}v^2 B_T \sin^6(\theta_c/2)$	0.53	0.69
$d\Phi_{MP}/dt$	$v^{4/3}B_T^{2/3} \sin^{8/3}(\theta_c/2)$	0.31	0.56

Figure 9. Scatterplots of (a, b) hemispheric precipitation rate and (c, d) hemispheric power of cusp soft electrons as a function of solar wind dynamic pressure derived from the Solstice Case for the Northern (Figures 9a and 9c) and Southern (Figures 9b and 9d) Hemispheres, respectively.

In the Solstice Case, the dynamic pressure is still the SW coupling function that has the highest linear correlation with the soft electron precipitation in the cusp region during tilted dipole conditions. The simulated linear regression relations between the hemispheric integrated rate/power of precipitating cusp soft electrons and SW dynamic pressure derived from the Solstice Case simulation are

$$\text{Power}_{\text{sum}} = (0.289 \pm 0.004)p - (0.070 \pm 0.011) \tag{5}$$

$$\text{Rate}_{\text{sum}} = (0.667 \pm 0.009)p - (0.278 \pm 0.023) \tag{6}$$

$$\text{Power}_{\text{win}} = (0.162 \pm 0.002)p + (0.050 \pm 0.006) \tag{7}$$

$$\text{Rate}_{\text{win}} = (0.339 \pm 0.005)p - (0.115 \pm 0.012) \tag{8}$$

where the subscript *sum* and *win* stand for the summer hemisphere and winter hemispheres, respectively.

Neither SW number density nor dynamic pressure was considered to have significant impact on predicting magnetospheric indices associated with the electrodynamic coupling between SW and magnetosphere in the literature (e.g., Newell et al., 2007). However, the simulation results suggest that the commonly used SW coupling functions, which involve the use of SW electric field, may not be the appropriate SW coupling functions describing the direct-entry of magnetosheath plasma into the I-T system. The simulation results suggest that the SW dynamic pressure gives the best correlation with the cusp soft electron precipitation. According to equations (1) and (2), the precipitating cusp electron number flux F_N can be linked to SW dynamic pressure through the relation $F_N = L_0 \frac{N_e T_e^{1/2}}{\sqrt{2\pi m_e}} \propto N_e V_{\text{the}} \propto n_{\text{sw}}^{1/2} p^{1/2}$, where V_{the} is the thermal velocity, which is proportional to $\sqrt{T_e/m_e}$. This indicates that the electron number flux is directly controlled by both the SW number density and dynamic pressure. Meanwhile, the electron energy flux F_E has the relation $F_E = 2F_N T_e \propto N_e V_{\text{the}}^3 \propto p^{3/2}n^{-1/2}$. Therefore, both the precipitating electron number flux and energy flux are closely related to the SW dynamic pressure. It should be pointed out that the integrated number flux F_N and energy flux F_E are also influenced by the size of the polar cusp, which is also controlled by the SW

Table 3
The Linear Correlation Between SW Coupling Functions and Cusp Soft Electron Hemispheric Precipitation Rate and Hemispheric Power Derived From the Solstice Case Simulation for Northern Hemisphere (NH) and Southern Hemisphere (SH)

Name	Function form	Hemispheric precipitation rate		Hemispheric power	
		NH	SH	NH	SH
B_z	B_z	0.48	0.06	0.37	0.02
Velocity	v	0.21	0.15	0.37	0.26
Density	n	0.79	0.87	0.73	0.80
p	$nv^2/2$	0.85	0.87	0.85	0.84
B_s	$B_z \quad (B_z < 0)$	0.04	−0.27	−0.08	−0.33
	$0 \quad (B_z > 0)$				
Half-wave rectifier	vB_s	0.03	−0.26	−0.10	−0.34
ε	$vB^2 \sin^4 (\theta_c/2)$	0.14	0.44	0.29	0.53
ε_1	$vB_T^2 \sin^4 (\theta_c/2)$	0.14	0.44	0.29	0.53
ε_2	$vB \sin^4 (\theta_c/2)$	0.01	0.32	0.15	0.41
Solar wind E field	vB_T	0.74	0.60	0.82	0.66
E_{KL}	$vB_T \sin^2 (\theta_c/2)$	0.12	0.43	0.29	0.53
$E_{KL}^{1/2}$	$[vB^2 \sin^2 (\theta_c/2)]^{1/2}$	0.09	0.38	0.25	0.47
E_{KLV}	$v^{4/3}B_T \sin^2 (\theta_c/2)p^{1/6}$	0.20	0.52	0.38	0.62
E_{WAV}	$vB_T \sin^4 (\theta_c/2)$	0.01	0.32	0.15	0.41
E_{WAV}^2	$[vB_T \sin^4 (\theta_c/2)]^2$	0.07	0.32	0.20	0.40
$E_{WAV}^{1/2}$	$[vB_T \sin^4 (\theta_c/2)]^{1/2}$	−0.07	0.27	0.08	0.35
E_{WV}	$v^{4/3}B_T \sin^4 (\theta_c/2)p^{1/6}$	0.05	0.40	0.21	0.48
E_{SR}	$vB_T \sin^4 (\theta_c/2)p^{1/6}$	0.14	0.54	0.3	0.61
E_{TL}	$n^{1/2}v^2B_T \sin^6 (\theta_c/2)$	0.09	0.47	0.23	0.53
$d\Phi_{MP}/dt$	$v^{4/3}B_T^{2/3} \sin^{8/3} (\theta_c/2)$	−0.03	0.29	0.13	0.39

electric field. To provide a more accurate prediction of cusp soft electron precipitations from upstream SW driving conditions, pairs of coupling functions, which includes the electric field term, might be considered in a future study.

Note that we analyzed two event-based global magnetosphere simulations in this work. We have also performed two additional ideal simulations (not shown here) with fixed dipole tilt angle of 0° and 30° driven by fixed, moderate solar velocity and IMF conditions ($V = 400$ km/s, $B_z = −5$ nT) but with increasing solar wind density within 8 h. The results indicate that the idealized simulations with fixed dipole tilt angles give similar average ratios of N_{cusp}/N_{sw}, but with much less scattering in the data points due to the lack of variations in the upstream conditions. Therefore, it is more reasonable to use relatively long event simulations with realistic variabilities in the upstream driving conditions in order to validate the simulation results using statistical observations in Walsh et al. (2016).

4. Effect of Ionospheric Outflow

In this study, we assume there is no ionospheric plasma population from the inner boundary of LFM model. To test the possible influence of this assumption on the high-altitude cusp region, we did additional test simulations in order to see the effects of ionospheric outflow on the simulated N_{cusp}/N_{sw} results. Here we used the recently developed multifluid LFM (MFLFM)-Ionosphere Polar Wind Model (IPWM) driven by idealized SW/IMF conditions that may be representative to the simulation period above in order to see the role of ionospheric outflow on the direct entry of solar wind, especially the N_{cusp}/N_{sw} calculations together with pressure balance. The details about the IPWM code and the coupling processes within MFLFM-IPWM can be found in Varney et al. (2015, 2016a, 2016b).

The test simulations were driven by moderate SW/IMF conditions with $N_{sw} = 5$ cm^{-3}, $V = 400$ km/s, Cs = 40 km/s, and $B_z = −5$ nT. The solar $F_{10.7} = 80$ sfu corresponding to solar minimum conditions similar to
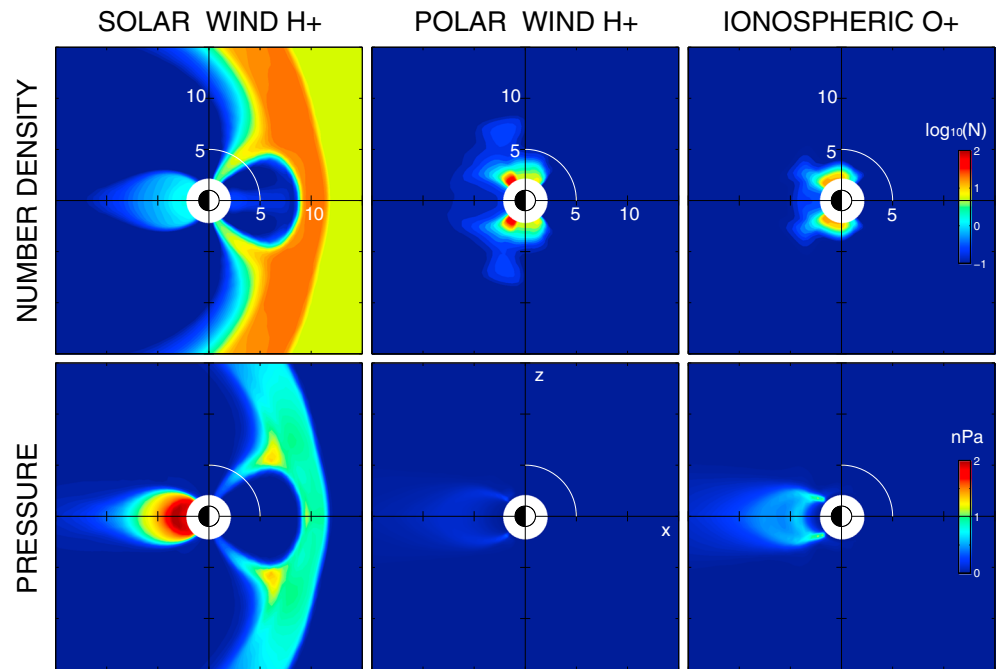
Figure 10. Average distributions of (top row) number density and (bottom row) thermal pressure of (left column) solar wind H$^+$, (middle column) ionospheric H$^+$, and (right column) ionospheric O$^+$ in the *x-z* plane (SM coordinates) derived from the last hour of the test simulation.
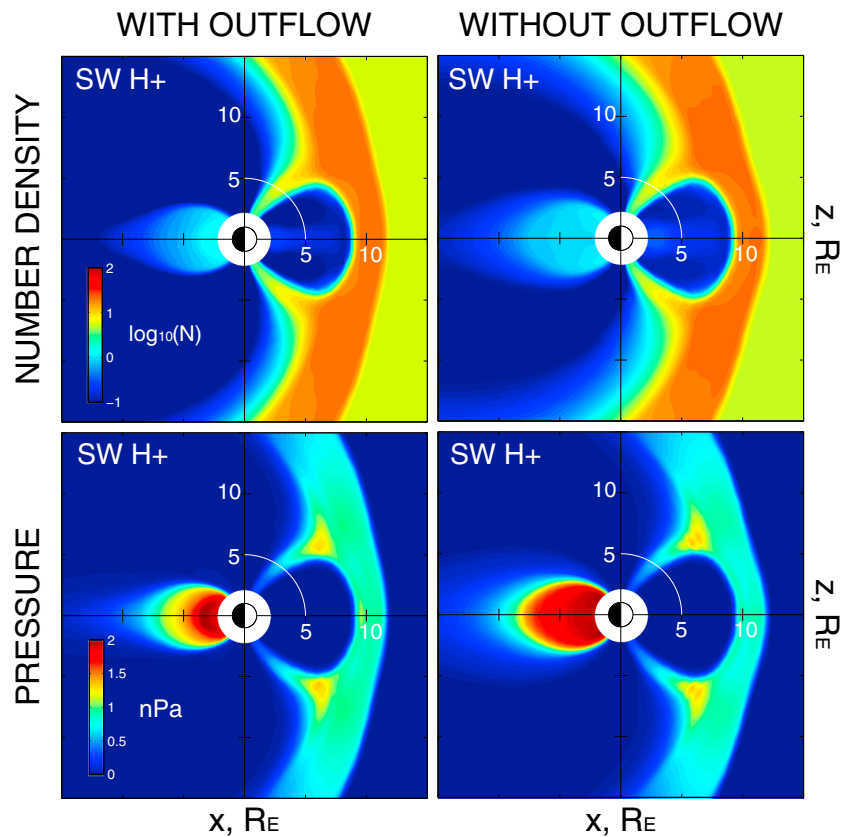

Figure 11. Average distributions of (top row) solar wind number density and (bottom row) pressure between the (left column) multifluid simulation with physics-based ionospheric outflow populations implemented and a (right column) single-fluid simulation without ionospheric outflow.
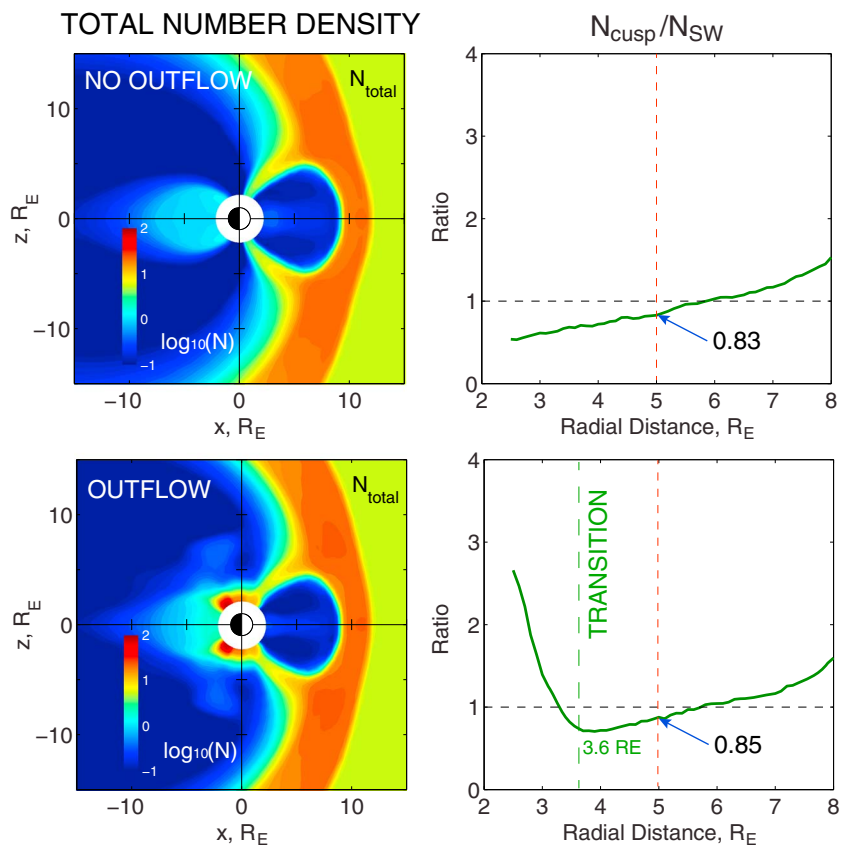
Figure 12. Average distributions of total plasma number density in the (left column) x-z plane and (right column) N_{cusp}/N_{sw} ratios derived from the two controlled simulations with and without ionospheric outflow.

the simulation event of Equinox Case. The model was preconditioned for 2 h southward IMF with $B_z = -5$ nT followed by 2 h northward IMF with $B_z = +5$ nT. Then IMF is switched to $B_z = -5$ nT for another 4 h. The simulation results presented in the following section are averaged from the last simulation hour.

The MFLFM-IPWM test simulation uses four fluids: solar wind H^+, polar wind H^+, polar wind O^+, and transversely accelerated (energetic) O^+. The details about a phenomenological wave-particle interactions model used in IPWM for energetic O^+ ion outflow together with the model validations are described in Varney et al. (2016a). Figure 10 shows the average distributions of number density and thermal pressure of the solar wind H^+, ionospheric H^+, and ionospheric O^+ in the x-z plane (SM coordinates) derived from the last hour of the test simulation. It is clear that at a radial distance of 5 R_E, both number density and pressure of the ionospheric ion populations are orders of magnitude lower than the solar wind H^+.

Figure 11 shows the comparisons on the solar wind number density and pressure between a single-fluid simulation (similar to the single-fluid simulation results analyzed in the previous section) and the multifluid simulation with physics-based ionospheric outflow populations implemented. While ionospheric outflow populations are included in the simulation, the shape of the magnetosphere changes as a consequence of system dynamics; for example, the location of the polar cusp moves slightly. Although the magnetotail is more influenced by the outflow population which has been demonstrated in previous simulation studies (e.g., Brambles et al., 2011), the entry of the solar wind plasma to low altitude is not significantly affected as shown in Figure 11, which is shown in the line plots in Figure 12.

Figure 12 displays the average distributions of total plasma number density in the x-z plane derived from the two controlled simulation with and without ionospheric outflow. The average ratio of the simulated N_{cusp}/N_{sw} as a function of radial distance is also calculated in Figure 12. It is evident that without ionospheric populations, the N_{cusp}/N_{sw} ratio increases with radial distance. At a radial distance of 5 R_E (shown by the red dashed line), the average N_{cusp}/N_{sw} ratio is approximately 0.83, which is consistent with the average value derived
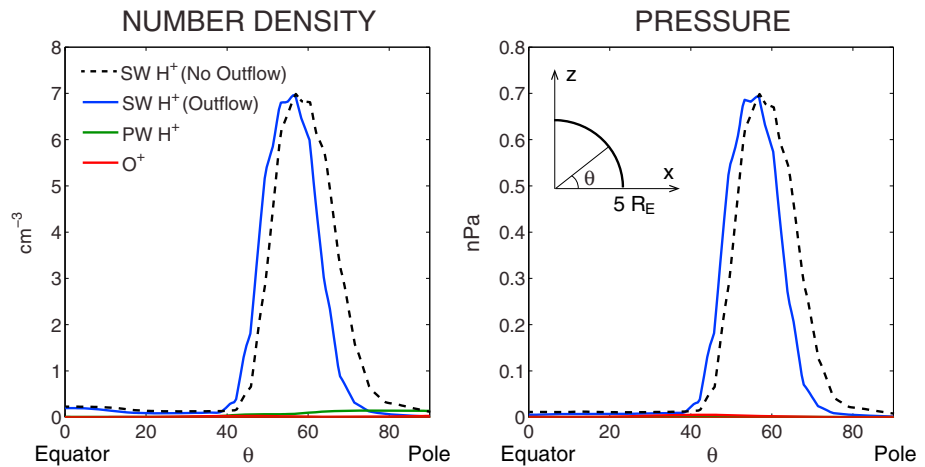
Figure 13. Distributions of number density and pressure of SW H$^+$, ionospheric H$^+$, and O$^+$ ions at a radial distance of 5 R_E in the x-z plane.

from the single-fluid simulation. When ionospheric populations are included in the simulation, the N_{cusp}/N_{sw} ratio changes significantly especially at radial distances smaller than 3.6 R_E (shown by the green dashed line). Near the radial distance of 1.5 R_E, the N_{cusp}/N_{sw} ratio is approximately 2.6, which is also consistent with Walsh et al. (2016). On the other hand, the N_{cusp}/N_{sw} ratio at a radial distance of 5 R_E derived from the simulation with outflow is approximately 0.85, which is close to the single-fluid simulation, suggesting that at radial distances larger than 5 R_E, the N_{cusp}/N_{sw} ratio is most likely dominated by the direct-entry of the solar wind H$^+$ rather than ionospheric H$^+$ or O$^+$. The simulated N_{cusp}/N_{sw} ratios in both simulations are consistent with Walsh et al. (2016) for radial distances greater than 5 R_E, regardless the present of ionospheric populations.

Figure 13 shows the distributions of number density and pressure of SW H$^+$, ionospheric H$^+$, and O$^+$ ions at a radial distance of 5 R_E in the x-z plane. It is again evident that at a radial distance of 5 R_E, the number density and pressure are dominated by the solar wind H$^+$ rather than ionospheric populations. Note that the magnitudes of the number density and pressure of SW H$^+$ remain about the same with ionospheric populations included, while the spatial distribution of the density and pressure shift toward high latitudes slightly (several degrees at a radial distance of 5 R_E) due to the global change of the magnetosphere state when ionospheric outflow populations are included in the simulation. This effect has been reported and studied in literature and is not the focus of our study.

To conclude, as shown in Figures 10–13, the coupled MFLFM-IPWM test simulation suggests that at a radial distance of 5 R_E (and above), ionospheric populations have relatively small contributions to the total plasma pressure and the simulated ratio of N_{cusp}/N_{sw} especially during quiet periods, which is consistent with Walsh et al. (2016). At radial distances smaller than 3.5 R_E, the ionospheric populations are important in order to make the N_{cusp}/N_{sw} ratio in agreement with observations. In addition, we have also looked at coupled IPWM-MFLFM simulations for $F_{10.7} = 200$ cases and found similar conclusions as shown in Figures 10–13. Therefore, ignoring ionospheric contributions to plasma populations at a radial distance of 5 R_E (and above) in the cusp region does not affect the simulated N_{cusp}/N_{sw} ratio derived from the simulations.

5. Summary

Predicting the cusp electron precipitation is important in investigating the dayside SW-magnetosphere-ionosphere coupling process and in forecasting space weather phenomena. The current global ionosphere/thermosphere circulation models usually calculate the impact of precipitating electrons by employing the empirical ionization models such as Lazarev (1967), Roble and Ridley (1987), and Frahm et al. (1997). For instance, The auroral particle precipitation is specified using the method of Roble and Ridley (1987) in the National Center for Atmospheric Research Thermosphere-Ionosphere-Electrodynamics General Circulation Model. However, the soft electron precipitations in the cusp region has been rarely considered in these empirical models. The aim of this paper is to find the optimal SW coupling function for describing the fluxes of

precipitating soft electrons in the polar cusp region and provide a possible empirical calculation for the fluxes of cusp soft electron precipitation based on the upstream solar wind driving conditions.

In this study, we use the LFM global simulation to investigate the correlation between the fluxes of precipitating electrons in the cusp and the upstream solar wind conditions. The simulations are run from 20 March 2008 to 16 April 2008 and from 15 to 24 December 2014, which are referred as Equinox Case and Solstice Case, respectively. For the Equinox Case, the mean plasma density ratio N_{cusp}/N_{sw} is 0.78, which agrees well with the statistical observations in Walsh et al. (2016). The effectiveness of 20 candidate SW coupling functions are examined for the linear correlation with the simulated number flux and energy flux of cusp soft electrons. The statistical results indicate that the solar wind dynamic pressure has the highest correlation coefficients with both hemispheric precipitation rate and hemispheric power of precipitating soft electrons. The linear regression relations between SW dynamic pressure p and cusp soft electrons at equinox for the hemispheric electron precipitation rate and power are Power $= (0.266p \pm 0.003) - (0.110 \pm 0.006)$, Rate $= (0.425p \pm 0.005) - (0.214 \pm 0.009)$.

We have also investigated the correlation between SW parameters and cusp soft electrons at solstice when the dipole tilt angle is large. The simulation results in Solstice Case show that the average plasma density ratio n_{cusp}/n_{sw} in the Southern (summer) Hemisphere is much larger than that in the Northern (winter) Hemisphere due to the large dipole tilt angle. The SW dynamic pressure p is still the highest correlated SW coupling function for both hemispheric precipitation rate and hemispheric power of soft electrons, with the correlation coefficients larger than 0.8. Thus, our results can be used to improve the specification of precipitating soft electrons in the cusp region in the ionosphere and thermosphere models.

References

Borovsky, J. E. (2013). Physical improvements to the solar wind reconnection control function for the Earth's magnetosphere. *Journal of Geophysical Research: Space Physics*, *118*, 2113–2121. https://doi.org/10.1002/jgra.50110

Brambles, O. J., Lotko, W., Zhang, B., Lyon, J., Wiltberger, M., & Strangeway, R. J. (2011). Magnetosphere sawtooth oscillations induced by ionospheric outflow. *Science*, *332*, 1183–1186. https://doi.org/10.1126/science.1202869

Burchill, J. K., Knudsen, D. J., Clemmons, J. H., Oksavik, K., Pfaff, R. F., Steigies, C. T., ... Yeoman, T. K. (2010). Thermal ion upflow in the cusp ionosphere and its dependence on soft electron energy flux. *Journal of Geophysical Research*, *115*, A05206. https://doi.org/10.1029/2009JA015006

Deng, Y., Fuller-Rowell, T. J., Ridley, A. J., Knipp, D., & Lopez, R. E. (2013). Theoretical study: Influence of different energy sources on the cusp neutral density enhancement. *Journal of Geophysical Research: Space Physics*, *118*, 2340–2349. https://doi.org/10.1002/jgra.50197

Eather, R. H. (1985). Polar cusp dynamics. *Journal of Geophysical Research*, *90*(A2), 1569–1576. https://doi.org/10.1029/JA090iA02p01569

Frahm, R. A., Winningham, J. D., Sharber, J. R., Link, R., Crowley, G., Gaines, E. E., ... Potemra, T. A. (1997). The diffuse aurora: A significant source of ionization in the middle atmosphere. *Journal of Geophysical Research*, *102*(D23), 28,203–28,214. https://doi.org/10.1029/97JD02430

Heikkila, W. J., & Winningham, J. D. (1971). Penetration of magnetosheath plasma to low altitudes through the dayside magnetospheric cusps. *Journal of Geophysical Research*, *76*(4), 883–891. https://doi.org/10.1029/JA076i004p00883

Kan, J. R., & Lee, L. C. (1979). Energy coupling function and solar wind-magnetosphere dynamo. *Geophysical Research Letters*, *6*(7), 577–580. https://doi.org/10.1029/GL006i007p00577

Lazarev, V. I. (1967). Absorption of the energy of an electron beam in the upper atmosphere. *Geomagnetism and Aeronomy*, *7*, 219.

Lyon, J. G., Fedder, J. A., & Mobarry, C. M. (2004). The Lyon-Fedder-Mobarry (LFM) global MHD magnetospheric simulation code. *Journal of Atmospheric and Solar-Terrestrial Physics*, *66*(15-16), 1333–1350. https://doi.org/10.1016/j.jastp.2004.03.020

McPherron, R. L., Hsu, T.-S., & Chu, X. (2015). An optimum solar wind coupling function for the *AL* index. *Journal of Geophysical Research: Space Physics*, *120*, 2494–2515. https://doi.org/10.1002/2014JA020619

Merkin, V. G., & Lyon, J. G. (2010). Effects of the low-latitude ionospheric boundary condition on the global magnetosphere. *Journal of Geophysical Research*, *115*, A10202. https://doi.org/10.1029/2010JA015461

Newell, P. T., Liou, K., Zhang, Y., Sotirelis, T., Paxton, L. J., & Mitchell, E. J. (2014). OVATION Prime-2013: Extension of auroral precipitation model to higher disturbance levels. *Space Weather*, *12*, 368–379. https://doi.org/10.1002/2014JA020769

Newell, P. T., Meng, C.-I., Sibeck, D. G., & Lepping, R. (1989). Some low-altitude cusp dependencies on the interplanetary magnetic field. *Journal of Geophysical Research*, *94*(A7), 8921–8927. https://doi.org/10.1029/JA094iA07p08921

Newell, P. T., Sotirelis, T., & Wing, S. (2009). Diffuse, monoenergetic, and broadband aurora: The global precipitation budget. *Journal of Geophysical Research*, *114*, A09207. https://doi.org/10.1029/2009JA014326

Newell, P. T., Sotirelis, T., Carbary, J. F., Liou, K., Skura, J. P., Meng, C.-I., ... Rich, F. J. (2002). OVATION: Oval variation, assessment, tracking, intensity, and online nowcasting. *Annales Geophysicae*, *20*, 1039–1047.

Newell, P. T., Sotirelis, T., Liou, K., Meng, C. I., & Rich, F. J. (2007). A nearly universal solar wind-magnetosphere coupling function inferred from 10 magnetospheric state variables. *Journal of Geophysical Research*, *112*, A01206. https://doi.org/10.1029/2006JA012015

Ogawa, Y., Fujii, R., Buchert, S. C., Nozawa, S., & Ohtani, S. (2003). Simultaneous EISCAT Svalbard radar and DMSP observations of ion upflow in the dayside polar ionosphere. *Journal of Geophysical Research*, *108*(A3), 1101. https://doi.org/10.1029/2002JA009590

Perreault, P., & Akasofu, S. I. (1978). A study of geomagnetic storms. *Geophysical Journal of the Royal Astronomical Society*, *54*(3), 547–573. https://doi.org/10.1111/j.1365-246X.1978.tb05494.X

Rentz, S. (2009). The upper atmospheric fountain effect in the polar cusp region (PhD thesis), Potsdam, Germany. https://doi.org/10.2312/GFZ.b103-09050

Roble, R., & Ridley, E. (1987). An auroral model for the NCAR thermospheric general circulation model (TGCM). *Annales Geophysicae*, *5*(A), 369–382.

Scurry, L., & Russell, C. T. (1991). Proxy studies of energy transfer to the magnetosphere. *Journal of Geophysical Research*, *96*(A6), 9541–9548. https://doi.org/10.1029/91JA00569

Skjæveland, Å, Moen, J., & Carlson, H. C. (2011). On the relationship between flux transfer events, temperature enhancements, and ion upflow events in the cusp ionosphere. *Journal of Geophysical Research*, *116*, A10305. https://doi.org/10.1029/2011JA016480

Smith, M. F., & Lockwood, M. (1996). Earth's magnetospheric cusps. *Reviews of Geophysics*, *34*(2), 233–260. https://doi.org/10.1029/96RG00893

Strangeway, R. J., Ergun, R. E., Su, Y. J., Carlson, C. W., & Elphic, R. C. (2005). Factors controlling ionospheric outflows as observed at intermediate altitudes. *Journal of Geophysical Research*, *110*, A03221. https://doi.org/10.1029/2004JA010829

Varney, R. H., Wiltberger, M., & Lotko, W. (2015). Modeling the interaction between convection and nonthermal ion outflows. *Journal of Geophysical Research: Space Physics*, *120*, 2353–2362. https://doi.org/10.1002/2014JA020769

Varney, R. H., Wiltberger, M., Zhang, B., Lotko, W., & Lyon, J. (2016a). Influence of ion outflow in coupled geospace simulations: 1. Physics-based ion outflow model development and sensitivity study. *Journal of Geophysical Research: Space Physics*, *121*, 9671–9687. https://doi.org/10.1002/2016JA022777

Varney, R. H., Wiltberger, M., Zhang, B., Lotko, W., & Lyon, J. (2016b). Influence of ion outflow in coupled geospace simulations: 2. Sawtooth oscillations driven by physics-based ion outflow. *Journal of Geophysical Research: Space Physics*, *121*, 9688–9700. https://doi.org/10.1002/2016JA022778

Vasyliunas, V. M., Kan, J. R., Siscoe, G. L., & Akasofu, S. I. (1982). Scaling relations governing magnetospheric energy transfer. *Planetary and Space Science*, *30*(4), 359–365. https://doi.org/10.1016/0032-0633(82)90041-1

Wahlund, J. E., Opgenoorth, H. J., Haggstrom, I., Kinser, K. J., & Jones, G. O. L. (1992). EISCAT observations of topside ionospheric ion outflows during auroral activity: Revisited. *Journal of Geophysical Research*, *97*(A3), 3019–3037. https://doi.org/10.1029/91JA02438

Walsh, B. M., Niehof, J., Collier, M. R., Welling, D. T., Sibeck, D. G., Mozer, F. S., . . . Kuntz, K. D. (2016). Density variations in the Earth's magnetospheric cusps. *Journal of Geophysical Research: Space Physics*, *121*, 2131–2142. https://doi.org/10.1002/2015JA022095

Welling, D. T., & Liemohn, M. W. (2014). Outflow in global magnetohydrodynamics as a function of a passive inner boundary source. *Journal of Geophysical Research: Space Physics*, *119*, 2691–2705. https://doi.org/10.1002/2013JA019374

Wygant, J. R., Torbert, R. B., & Mozer, F. S. (1983). Comparison of S3-3 polar cap potential drops with the interplanetary magnetic field and models of magnetopause reconnection. *Journal of Geophysical Research*, *88*(A7), 5727–5735. https://doi.org/10.1029/JA088iA07p05727

Zhang, B., Brambles, O., Lotko, W., Dunlap-Shohl, W., Smith, R., Wiltberger, M., & Lyon, J. (2013). Predicting the location of polar cusp in the Lyon-Fedder-Mobarry global magnetosphere simulation. *Journal of Geophysical Research: Space Physics*, *118*, 6327–6337. https://doi.org/10.1002/jgra.50565

Zhang, B., Lotko, W., Brambles, O., Wiltberger, M., Wang, W., Schmitt, P., & Lyon, J. (2012). Enhancement of thermospheric mass density by soft electron precipitation. *Geophysical Research Letters*, *39*, L20102. https://doi.org/10.1029/2012GL053519

Zhang, B., Lotko, W., Brambles, O., Wiltberger, M., & Lyon, J. (2015). Electron precipitation models in global magnetosphere simulations. *Journal of Geophysical Research: Space Physics*, *120*, 1035–1056. https://doi.org/10.1002/2014JA020615

Zhang, B., Varney, R. H., Lotko, W., Brambles, O. J., Wang, W., Lei, J., . . . Lyon, J. (2015). Pathways of F region thermospheric mass density enhancement via soft electron precipitation. *Journal of Geophysical Research: Space Physics*, *120*, 5824–5831. https://doi.org/10.1002/2015JA020999

Zhou, X. W., Russell, C. T., Le, G., Fuselier, S. A., & Scudder, J. D. (1999). The polar cusp location and its dependence on dipole tilt. *Geophysical Research Letters*, *26*(3), 429–432. https://doi.org/10.1029/1998GL900312